JOURNAL OF GEOPHYSICAL RESEARCH, VOL. 106, NO. C6, PAGES 11,639–11,651, JUNE 15, 2001

Properties of the water column and bottom derived from Airborne Visible Infrared Imaging Spectrometer (AVIRIS) data

Zhongping Lee, Kendall L. Carder, Robert F. Chen, and Thomas G. Peacock

Department of Marine Science, University of South Florida, St. Petersburg, Florida

Abstract. Using Airborne Visible Infrared Imaging Spectrometer (AVIRIS) data as an example, we show in this study that the properties of the water column and bottom of a large, shallow area can be adequately retrieved using a model-driven optimization technique. The simultaneously derived properties include bottom depth, bottom albedo, and water absorption and backscattering coefficients, which in turn could be used to derive concentrations of chlorophyll, dissolved organic matter, and suspended sediments in the water column. The derived bottom depths were compared with a bathymetry chart and a boat survey and were found to agree very well. Also, the derived bottom albedo image shows clear spatial patterns, with end-members consistent with sand and seagrass. The image of absorption and backscattering coefficients indicates that the water is quite horizontally mixed. Without bottom corrections, chlorophyll *a* retrievals were ~50 mg m^{-3}, while the retrievals after bottom corrections were tenfold less, approximating real values. These results suggest that the model and approach used work very well for the retrieval of subsurface properties of shallow-water environments even for rather turbid environments like Tampa Bay, Florida.

1. Introduction

Remote sensing by aircraft or satellite has been proven to be very useful for quickly providing important environmental information over large areas. However, owing to research priorities or technical limitations most such remote-sensing applications have been focused on open ocean and offshore waters. Nearshore waters, owing to complexities ranging from land runoff to bottom reflection, have been studied less often using satellite imagery. The presence of bottom-reflected light obviates the utility of most empirical algorithms for retrieving properties of the water column (e.g., chlorophyll and absorption coefficients), while then scattering and attenuation of incident light by the water complicates retrievals of bottom depth and albedo. However, near-shore waters are important for our quality of life, and at the same time, near-shore environments are under continuous stress due to human activities and natural events. Methods and techniques are needed to monitor the properties of near-shore waters as well as the condition of benthic ecosystems such as seagrass beds.

In the earlier coastal studies, bottom depth and albedo retrievals from satellite images required many assumptions to be made [e.g., *Clark et al.*, 1987; *Lyzenga*, 1985; *Zhang et al.*, 1999] or ancillary ground truth data. These procedures may be appropriate for a given study location, but they often are not for other shallow regions. A more universal, reliable, and practical technique is desired for the retrieval of properties of shallow, near-shore environments from spectral imagery.

Paper number 2000JC000554.
0148-0227/01/2000JC000554$09.00

On the basis of a recent semianalytical model for shallow-water remote sensing [*Lee et al.*, 1998], *Lee et al.* [1999] showed that underwater information such as bottom depth and water column properties could be analytically and simultaneously derived from hyperspectral data using an optimization approach. In the process, no data were used except the measured remote-sensing reflectance. The retrieved depths agreed with the true depths within 8% for a range from 2 to 25 m for waters of the west Florida shelf, the Florida Keys, and the Bahamas [*Lee et al.*, 1999]. These kinds of results provide confidence that properties of submerged coastal environments such as bathymetry, water quality parameters (e.g., absorption and clarity), and bottom albedo can be derived just from passive hyperspectral data as long as the data have an adequate signal-to-noise ratio and the water column is well mixed. However, it is not known yet how this technique would perform for spectral images of a more complicated environment.

In this study, using Airborne Visible Infrared Imaging Spectrometer (AVIRIS) data over the Tampa Bay (Florida) estuary, we show that the model-driven optimization technique [*Lee et al.*, 1999] can be applied to spectral images of shallow and turbid coastal waters to adequately retrieve underwater information without a priori knowledge of the optical properties of the water column or bottom reflectivity or depth.

2. AVIRIS Data

The Airborne Visible Infrared Imaging Spectrometer of Jet Propulsion Laboratory is a test bed for future spacecraft imaging spectrometers [*Green*, 1999]. It has 224 spectral channels from 400 to 2400 nm and a 4 m x 4 m spatial resolution when viewing from an altitude of 3810 m. In the past decade, many land and oceanic applications were carried

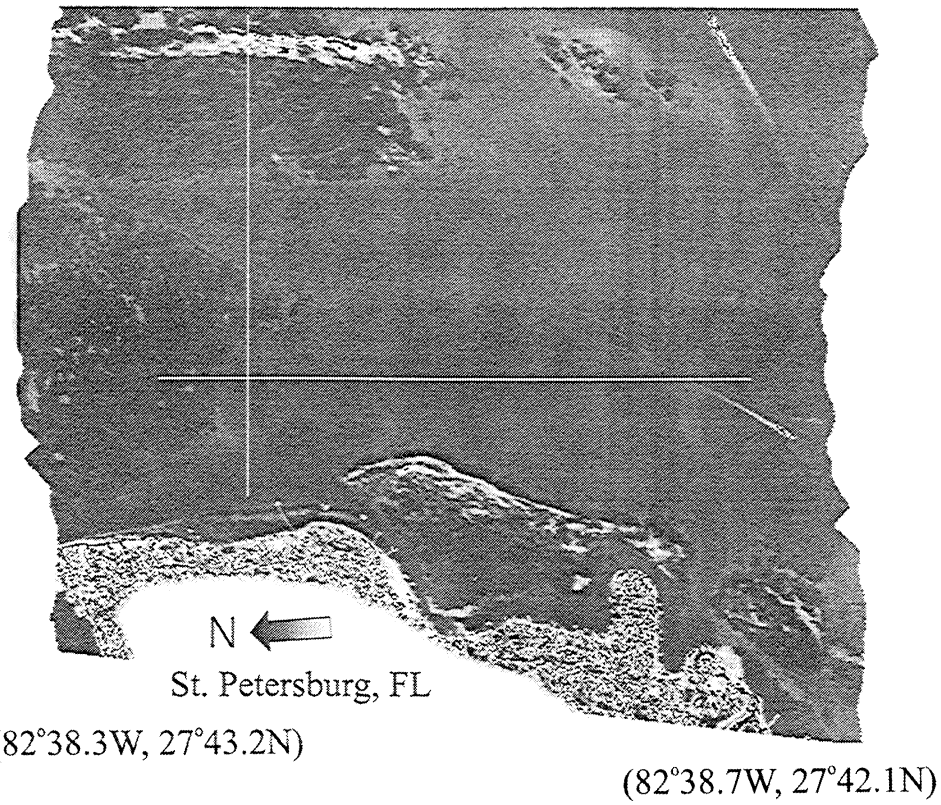

Figure 1. The study area.

out using AVIRIS data [e.g., *Green*, 1999; *Carder et al.*, 1993a, 1993b; *Hamilton et al.*, 1993].

Low-altitude AVIRIS data over Tampa Bay (Florida) were collected from a Twin-Otter aircraft flying at 3810 m altitude on November 18, 1998, at 1200 local time. Figure 1 shows the study area. The AVIRIS radiance calibration and atmospheric correction were performed vicariously using the method of *Carder et al.* [1993a], which consisted of comparing modeled upwelling radiance at the aircraft altitude to AVIRIS data at a relatively uniform site (~5 km away from this image) where the water-leaving radiance was measured. Briefly, the atmospheric radiance was calculated by MODTRAN4 at the AVIRIS altitude using a midlatitude winter model with a maritime extinction aerosol type. By adjusting visibility of the model to match the total AVIRIS radiance at 807 nm the modeled atmospheric radiance was finalized for the vicarious calibration site. We then initially assumed the aerosols to be horizontally homogeneous in their properties for the entire AVIRIS transect. For this low-altitude AVIRIS data, typically, we observed water leaving radiance values of ~30% of the total sensor signal at 550 nm. After atmospheric correction, the ratio of the calculated water-leaving radiance to MODTRAN4-calculated downwelling total irradiance at the surface provided initial remote-sensing reflectance $R_{rs}^{i}(\lambda)$ curves. To overcome effects of nonhomogeneity in aerosol properties and errors in atmospheric correction, a first-order adjustment to the above $R_{rs}^{i}(\lambda)$ values was carried out in a manner similarly to that of *Arnone et al.* [1998]. (1) $R_{rs}^{i}(\lambda)$ is biased to make $R_{rs}^{i}(750) = 0$ and get $R_{rs}^{1}(\lambda) = R_{rs}^{i}(\lambda) - R_{rs}^{i}(750)$; (2) on the basis of an empirical relationship from ship-borne data, $R_{rs}(750)$ was estimated from $R_{rs}^{1}(650)$, $R_{rs}(750) = 0.0001 + 0.02\, R_{rs}^{1}(650)$; (3) finally, we get $R_{rs}(\lambda) = R_{rs}^{1}(\lambda) + R_{rs}(750)$. This $R_{rs}(\lambda)$ is then used as input in the following remote sensing inversion.

From Figure 1 it is easy to imagine that the study area is very complicated, with distinct patterns from left to right. However, without further analysis, it is difficult to tell what causes the spatial variation since it may result from changes in bottom depth (deep versus shallow), bottom substrate (sand versus seagrass), and/or water turbidity. Traditional approaches typically avoid regions like this because of a lack of knowledge of the water column contributions, the attenuation coefficients, and bottom albedos. We apply here a newly developed shallow-water inversion scheme [*Lee et al.*, 1999] to this complicated environment. The white horizontal line in Figure 1 indicates the route of a bathymetric survey, from which the measured bottom depths were used for comparison with AVIRIS derived depths. The white vertical line in Figure 1 is selected to show the bottom influence on empirical retrieval of chlorophyll *a* concentrations.

Also measured at the AVIRIS calibration site were the chlorophyll *a* concentration and water absorption coefficients from bucket samples using methods described in the Sea-viewing Wide Field-of-view Sensor (SeaWiFS) protocols [*Mueller and Austin*, 1992]. The chlorophyll *a* concentration was 5.0 mg m^{-3}, and the absorption coefficient at 440 nm of 0.9 m^{-1}. This was a sum of absorption of pure water [*Pope and Fry*, 1997], particle, and gelbstoff (yellow substance or colored dissolved organic matter).

3. Inverting Remote-Sensing Reflectance R_{rs}

Remote-sensing reflectance R_{rs} is an apparent optical property [*Preisendorfer*, 1976], controlled by the absorption coefficients, scattering properties, and the bottom albedo and bottom depth. It is also influenced by fluorescence and Raman

emission [*Marshall and Smith*, 1990; *Lee et al.*, 1994] and by the angles of solar input and output radiance [*Morel and Gentili*, 1993]. For waters with vertical homogeneity and ignoring the inelastic scattering contributions,

$$R_{rs}(\lambda) = f[a(\lambda), b_b(\lambda), \rho(\lambda), H, \theta_w, \theta_v, \varphi], \quad (1)$$

where $a(\lambda)$ is the absorption coefficient, $b_b(\lambda)$ is the backscattering coefficient, $\rho(\lambda)$ is the bottom albedo, H is the bottom depth, θ_w is the subsurface solar zenith angle, θ_v is the subsurface viewing angle from nadir, and φ is the viewing azimuth angle from the solar plane. For brevity, wavelength dependence may not be explicitly included unless required for clarity.

In order to retrieve the bottom depth the water column contributions and optical properties of the water column have to be known or derived. Historically, values for water column contributions were approximated from values of adjacent deep waters [e.g., *Polcyn et al.*, 1970; *Lyzenga*, 1978, 1981; *O'Neill and Miller*, 1989], and light attenuation values were assumed known a priori [e.g., *Polcyn et al.*, 1970; *Paredes and Spero*, 1983] or empirically derived from an image by regression using a few true depths provided by lidar or on-site ship measurements [*Lyzenga*, 1985; *Philpot*, 1989]. All of these methods require knowledge of a few actual depths or accurate attenuation values. This suggests that if neither of those conditions is met, bottom depth cannot be accurately derived.

To be able to derive properties of shallow-water environments routinely, it is desired to simultaneously derive bottom depth and albedo and the optical properties of the water column. The model-driven optimization technique developed by *Lee et al.* [1999] demonstrated that most of the underwater information could be derived from the measured remote-sensing reflectance.

For $\varphi = 90°$ the semianalytical model (SA model) for R_{rs} is [*Lee et al.*, 1999]

$$R_{rs} \approx \frac{0.5 r_{rs}}{1 - 1.5 r_{rs}},$$

$$r_{rs} \approx r_{rs}^{dp}\left[1 - \exp\left(-\left(\frac{1}{\cos(\theta_w)} + \frac{D_u^C}{\cos(\theta_v)}\right)\kappa H\right)\right] + \frac{1}{\pi}\rho \exp\left(-\left(\frac{1}{\cos(\theta_w)} + \frac{D_u^B}{\cos(\theta_v)}\right)\kappa H\right), \quad (2)$$

$$r_{rs}^{dp} \approx (0.084 + 0.170u)\,u. \quad (3)$$

Here r_{rs} is the subsurface remote-sensing reflectance, or ratio of the upwelling radiance to downwelling irradiance evaluated just below the surface, and $r^{dp}{}_{rs}$ is the remote-sensing reflectance for optically deep waters.

The first term on the right side of the r_{rs} equation expresses the truncation of the path radiance expected for presence of a black bottom at depth H, while the second term expresses the bottom contribution at the surface after attenuated by the two-way path through the water column.

In (2) there are two optical path elongation factors: one for photons from the water column ($D^C{}_u$) and the other for photons from bottom ($D^B{}_u$). These are approximated as [*Lee et al.*, 1999]

$$D^C{}_u \approx 1.03(1+2.4u)^{0.5} \quad D^B{}_u \approx 1.04(1+5.4u)^{0.5}. \quad (4)$$

Here u and κ in (2)-(4) are defined as

$$u = b_b/(a+b_b) \qquad \kappa = a + b_b, \quad (5)$$

$$b_b = b_{bw} + b_{bp}, \quad (6)$$

$$a = a_w + a_\phi + a_g. \quad (7)$$

Note that both u and κ are inherent optical properties, and it is the combination of (2)-(7) that provides the expression for R_{rs}. In (2), 0.5/(1-1.5 r_{rs}) is the water-to-air divergence factor [*Gordon et al.*, 1988; *Mobley*, 1994], and (1-1.5 r_{rs}) accounts for the internal reflection of the water-air interface, which is important when r_{rs} values get high for very shallow and/or very turbid waters. Here b_{bw} is the backscattering coefficient of pure seawater, while b_{bp} is the backscattering coefficient of suspended particles; a_ϕ is the absorption coefficient for phytoplankton pigments, and a_g is the absorption coefficient for gelbstoff and detritus [*Carder et al.*, 1991].

When $R_{rs}(\lambda)$ is known, remote determination of subsurface properties is a mathematical process: spectrally decomposing (2) and accurately deriving the quantities of interest. For n independent channels of $R_{rs}(\lambda)$, (2) is a series of equations:

$$\begin{aligned} R_{rs}(\lambda_1) &= F(a_w(\lambda_1), b_{bw}(\lambda_1), a_\phi(\lambda_1), a_g(\lambda_1), b_{bp}(\lambda_1), \rho(\lambda_1), H) \\ R_{rs}(\lambda_2) &= F(a_w(\lambda_2), b_{bw}(\lambda_2), a_\phi(\lambda_2), a_g(\lambda_2), b_{bp}(\lambda_2), \rho(\lambda_2), H) \\ &\vdots \\ R_{rs}(\lambda_n) &= F(a_w(\lambda_n), b_{bw}(\lambda_n), a_\phi(\lambda_n), a_g(\lambda_n), b_{bp}(\lambda_n), \rho(\lambda_n), H), \end{aligned} \quad (8)$$

i.e., each measured $R_{rs}(\lambda)$ spectrum consists of at least four unknown spectra ($a_\phi(\lambda)$, $a_g(\lambda)$, $b_{bp}(\lambda)$, and $\rho(\lambda)$) and one scalar unknown (H), assuming the values of $a_w(\lambda)$ and $b_{bw}(\lambda)$ are known [*Pope and Fry*, 1997; *Morel*, 1974]. This suggests that for n equations, there are ($4n$ + 1) unknowns to be deduced. In order to solve for this many unknowns, additional relationships have to be established to reduce the number of unknowns (or increase the number of equations).

Here $a_\phi(\lambda)$ is simulated by a single-parameter model [*Lee et al.*, 1998]:

$$a_\phi(\lambda) = [a_0(\lambda) + a_1(\lambda)\ln(P)]\,P, \quad (9)$$

with $P = a_\phi(440)$, the variable for phytoplankton absorption coefficient at 440 nm. This approach allows $a_\phi(\lambda)$ curvature to change with $a_\phi(440)$ value, consistent with field observations, at least to first order. Values for $a_0(\lambda)$ and $a_1(\lambda)$ are provided in Table 1.

Here $a_g(\lambda)$ is expressed as [*Bricaud et al.*, 1981; *Roesler et al.*, 1989; *Carder et al.*, 1989]

$$a_g(\lambda) = G\,e^{-S(\lambda-440)}, \quad (10)$$

with $G = a_g(440)$. S is the spectral slope, and a value of 0.015 nm^{-1} is used as a representative average in our inversion process. This S value as well as $a_0(\lambda)$ and $a_1(\lambda)$ values can be replaced if site-specific knowledge is available.

Here $b_{bp}(\lambda)$ is expressed as

$$b_{bp}(\lambda) = X\left(\frac{400}{\lambda}\right)^Y, \quad (11)$$

where $X = b_{bp}(400)$, which is an effective particle backscattering coefficient as solar zenith angle and sensor viewing angle were also imbedded in the parameterization [*Lee et al.*, 1999]. In other words, it includes some small

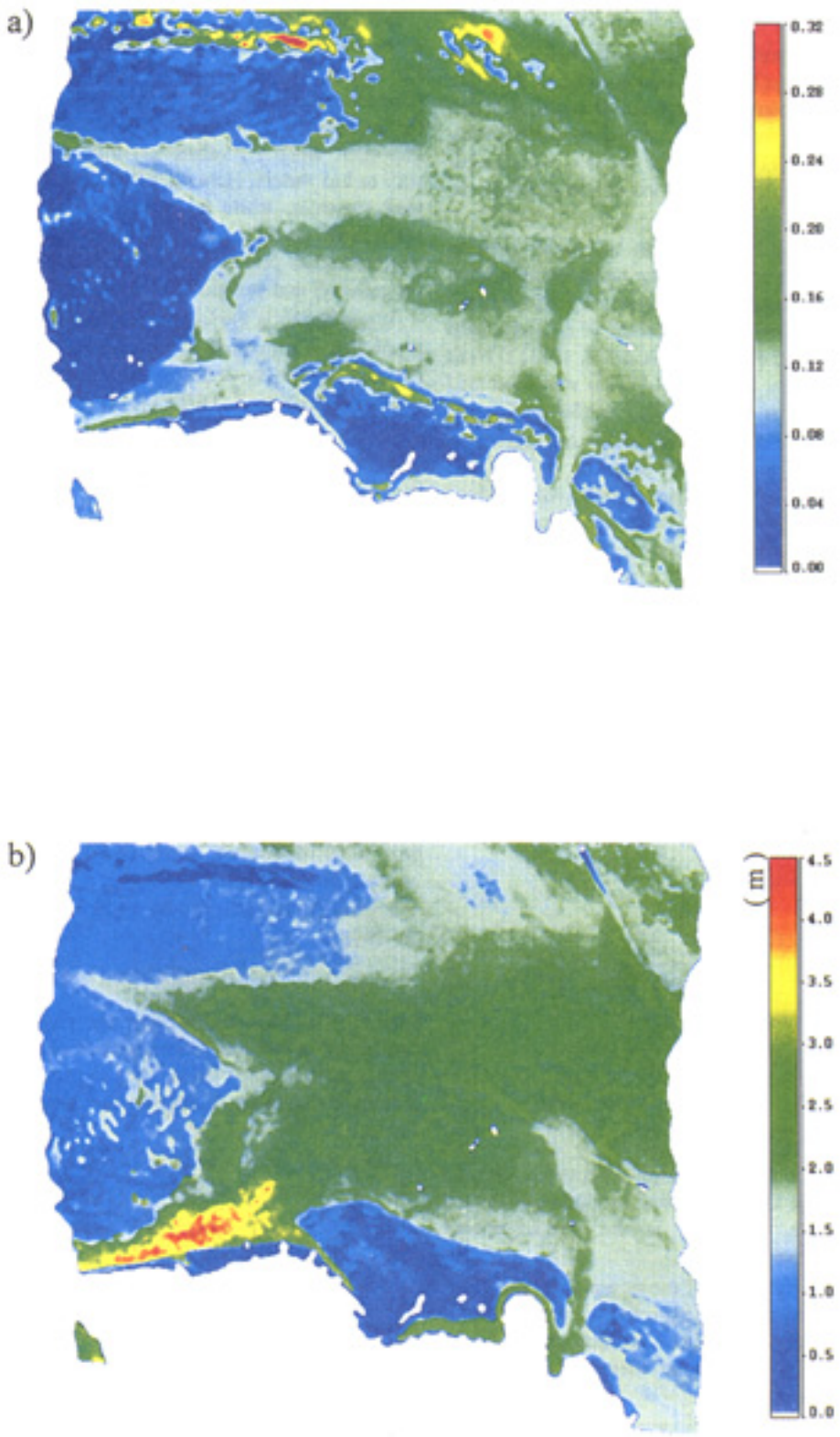

Plate 1. (a) Image of derived bottom albedo at 550 nm. (b) Image of derived bottom depth in meters.

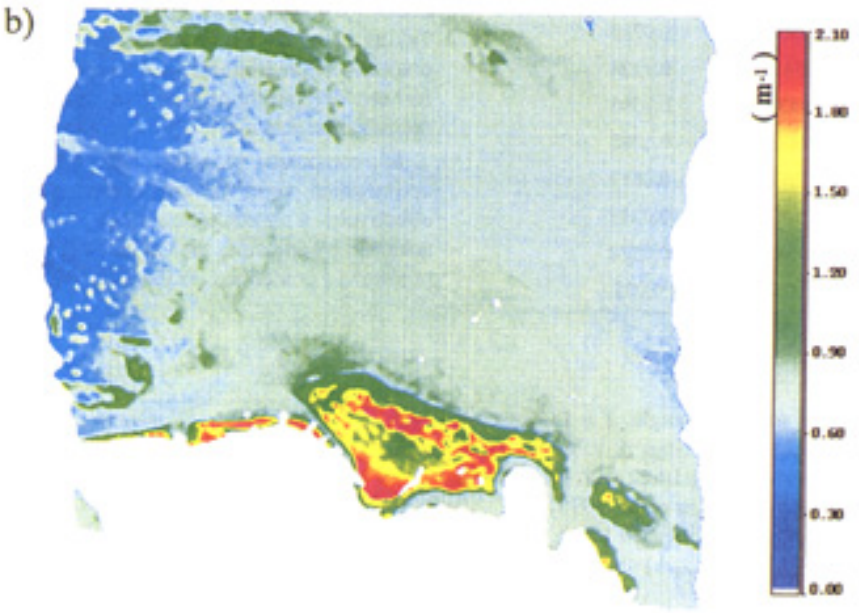

Plate 2. (a) Image of depth comparison. Lines are the isobaths from NOAA chart. Depths are in feet for comparison (1 foot = 0.3048 m). (b) Image of derived absorption coefficient at 440 nm.

Table 1. Parameters for the Empirical $a_\phi(\lambda)$ Simulation[a]

Wavelength	$a_0(\lambda)$	$a_1(\lambda)$
390	0.5813	0.0235
400	0.6843	0.0205
410	0.7782	0.0129
420	0.8637	0.006
430	0.9603	0.002
440	1.0	0
450	0.9634	0.006
460	0.9311	0.0109
470	0.8697	0.0157
480	0.789	0.0152
490	0.7558	0.0256
500	0.7333	0.0559
510	0.6911	0.0865
520	0.6327	0.0981
530	0.5681	0.0969
540	0.5046	0.09
550	0.4262	0.0781
560	0.3433	0.0659
570	0.295	0.06
580	0.2784	0.0581
590	0.2595	0.054
600	0.2389	0.0495
610	0.2745	0.0578
620	0.3197	0.0674
630	0.3421	0.0718
640	0.3331	0.0685
650	0.3502	0.0713
660	0.561	0.1128
670	0.8435	0.1595
680	0.7485	0.1388
690	0.389	0.0812
700	0.136	0.0317
710	0.0545	0.0128
720	0.025	0.005

[a] From *Lee* [1994].

effects of phase function on scattering angle. Y is the spectral shape parameter of particle backscattering. A value of 0.5 is used for all the pixels of this study, consistent with more turbid waters [*Sathyendranath et al.*, 1989; *Lee et al.*, 1999].

The parameter $\rho(\lambda)$ is expressed using 550 nm-normalized, sand albedo $\rho_{sand}(\lambda)$ or grass albedo $\rho_{grass}(\lambda)$ shapes (see Figure 2), i.e.,

$$\rho(\lambda) = B\,\rho_{sand}(\lambda) \quad \text{or} \quad \rho(\lambda) = B\,\rho_{grass}(\lambda), \tag{12}$$

where B is the bottom albedo value at 550 nm. Here $\rho_{sand}(\lambda)$ and $\rho_{grass}(\lambda)$ were from earlier field measurements (*Z. Lee et al.*, unpublished data, 1992). We used the following empirical criteria to initially separate sand from grass bottoms: if $R_{rs}(\lambda)$ of a pixel satisfies

$$R_{rs}(550) < 0.01 \quad \text{and} \quad R_{rs}(710)/R_{rs}(670) > 1.2,$$

spectral shape of ρ_{grass} is used; otherwise, spectral shape of ρ_{sand} is used.

After the above empirical/semianalytical models are assembled, (8) becomes

$$\begin{aligned} R_{rs}(\lambda_1) &= F(a_w(\lambda_1), b_{bw}(\lambda_1), P, G, X, B, H) \\ R_{rs}(\lambda_2) &= F(a_w(\lambda_2), b_{bw}(\lambda_2), P, G, X, B, H) \\ &\vdots \\ R_{rs}(\lambda_n) &= F(a_w(\lambda_n), b_{bw}(\lambda_n), P, G, X, B, H). \end{aligned} \tag{13}$$

There are only five variables for (13): P, G, X, B, and H. These five variables uniquely influence the $R_{rs}(\lambda)$ spectrum, which avoids the possibility of a singularity arising from (13), unless the data are very noisy.

The final question now is how to mathematically derive the five unknowns from known $R_{rs}(\lambda)$ spectrum. Theoretically, we only need five independent channels to solve for five unknowns. However, (13) is neither 100% accurate nor 100% complete in modeling the remote-sensing reflectance spectra of real environments, even if we have perfect sensors and atmospheric corrections. For example, it lacks terms for fluorescence of pigments, fluorescence of colored dissolved organic matter, and Raman scattering. Also, the empirical, bio-optical models used are not guaranteed to perfectly match the waters under study. All of these missing components are present, though mostly small, in the measured data, and distributed unevenly across the spectrum. Also, the wavelength of maximum bottom contribution depends on the wavelength of maximum transparency, which varies as a function of absorption and scattering. Since the values of absorption and scattering vary from place to place, it is hard to know a priori which wavelength contains the maximum bottom contribution. Figure 3 shows examples of measured remote-sensing reflectance, where one spectrum has maximum reflectance ~480 nm and another has ~570 nm. Thus it is difficult to determine the best five channels to be used for the derivation. Taking all of the above uncertainties into consideration, it is a practical and reasonable idea to apply all the useable channels for the derivation of the five unknowns by means of an optimization scheme.

A computer program has been developed for the optimization used in the inversion. This optimization is effectively a predictor-corrector, model-inversion scheme, achieved by adjusting the values of P, G, X, B, and H in (13) to minimize a predefined err function, which is

$$\text{err} = \frac{\left[\sum_{400}^{675}\left(R_{rs} - \hat{R}_{rs}\right)^2 + \sum_{750}^{800}\left(R_{rs} - \hat{R}_{rs}\right)^2\right]^{0.5}}{\sum_{400}^{675} R_{rs} + \sum_{750}^{800} R_{rs}}, \tag{14}$$

with $\hat{R}_{rs}$ for values from (13) and R_{rs} for values from AVIRIS. The cutoff between 675 and 750 nm is because no term is included in the model to express the solar-stimulated chlorophyll fluorescence presented in the measured data. Also, this spectral range is greatly affected by the absorption of water vapor that is quite variable. The computer program automatically changes the values of P, G, X, B, and H until err reaches a minimum. At that point, values for P, G, X, B, and H are then considered to be derived. In the process, P, G, X, B, and H are initiated at 0.2, 0.5, 0.01, 0.05, and 2.5, respectively, and are all kept positive. Note that no field data are

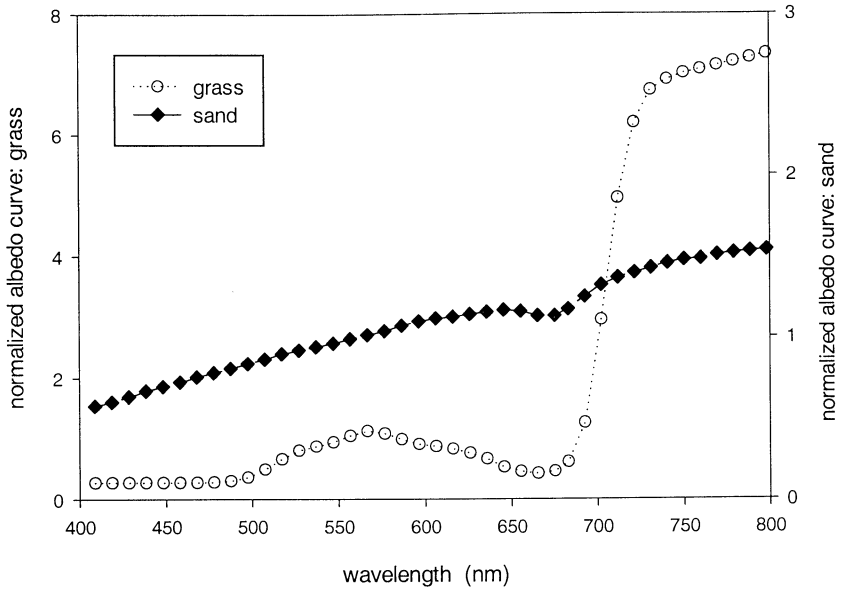

Figure 2. The spectra shapes of sand and seagrass bottom albedo used in this study.

required/used except the measured $R_{rs}(\lambda)$ curves. Knowledge of time- and space-dependent regional values for S, $a_0(\lambda)$ and $a_1(\lambda)$ values, however, can improve retrieval quality for a given site and season.

4. Results

Using a Pentium 400 Mhz, personal computer, the 630 x 510 (>300,000 pixels) AVIRIS image was processed in ~6 hours. It is not as fast as empirical regression algorithms, but it provides much more accurate retrievals for not only depth but also bottom albedo and water optical properties. The 6 hours of processing time is manageable if we are just processing a few images. For a large number of images, increased numbers of computers or more powerful computers can alleviate the computational burden caused by the optimization technique. The computed results are shown in Figures 4-9.

Figure 4 shows examples of modeled and AVIRIS-retrieved $R_{rs}(\lambda)$ curves for some selected pixels. The modeled $R_{rs}(\lambda)$ curves match AVIRIS $R_{rs}(\lambda)$ very well, suggesting that the calibration and atmospheric correction were quite good, leaving very little residual noise in the $R_{rs}(\lambda)$ spectra. Note that the difference ~685nm is due to chlorophyll *a* fluorescence in the AVIRIS data.

Plate 1a shows the image of derived bottom albedo at 550 nm, which shows clear spatial patterns, as clearly depicted by the two modes of its histogram (Figure 5). The bottom albedo values ranged from 0.02 to 0.2, with a few pixels around 0.3 (Plate 1a, top left). These values are consistent with values ranging from shaded grass canopies to those expected for

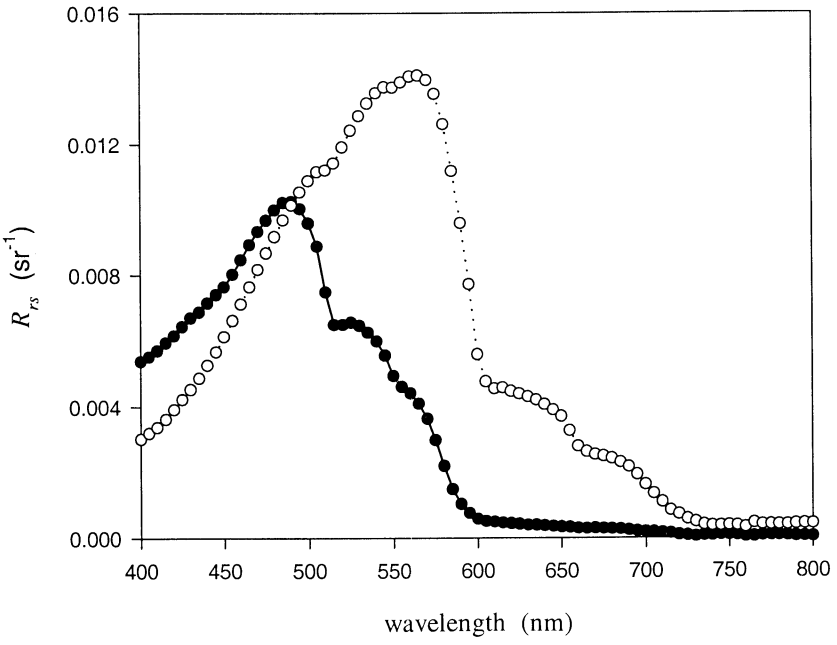

Figure 3. Examples of measured remote-sensing reflectance of two sandy bottoms.

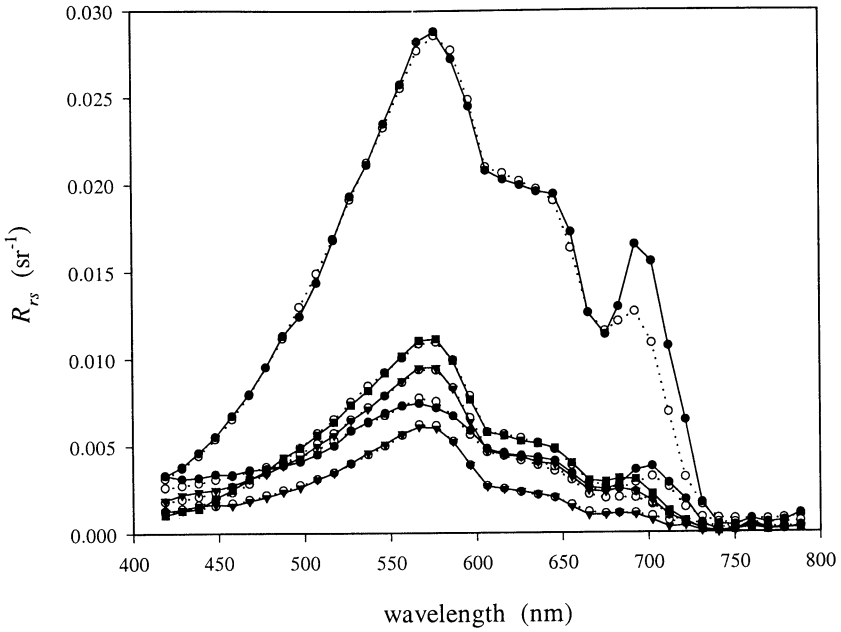

Figure 4. Examples of AVIRIS measured and modeled remote-sensing reflectance of this study.

sandy bottoms [*Hou et al.*, 2000]. If we set a criteria such that albedo values <5% are seagrass and >10% are muddy quartz sand, then this image suggests that seagrass occupies the left side, and sand occupies the right side of the image. At the top left, there is a strip of a sandy bar.

Plate 1b shows the image of derived bathymetry, ranging from ~0.3 to 4.6 m, with the deepest place in the left lower corner. The upper left part of the image is much shallower, with depths around 0.6-1.2 m, and in the middle of the image the depths are ~2.4 m.

To see how the derived depths compared with earlier known depths, we scanned a bathymetry chart (National Oceanic and Atmospheric Administration (NOAA) No.11414) into an image and superimposed it on the AVIRIS depth image, as shown by Plate 2a. The depths in the chart were surveyed before 1978, and values were for mean lower low water. In Plate 2a the lines are the isobaths from the chart. To make the two depth charts comparable, the AVIRIS-derived depths were converted from meters to feet (1 foot = 0.3048 m). The water was in the middle of a rising tide when AVIRIS was collecting imagery, so we subtracted 1.3 feet from the AVIRIS-derived depths to make it comparable with chart depths. By comparing the two depth images, there are some interesting findings: (1) Both charts show that the deepest places are at the lower left corner (marked A), with depth values around 14 feet (4.6 m). Also, both charts show the shallowest places are at the sandy

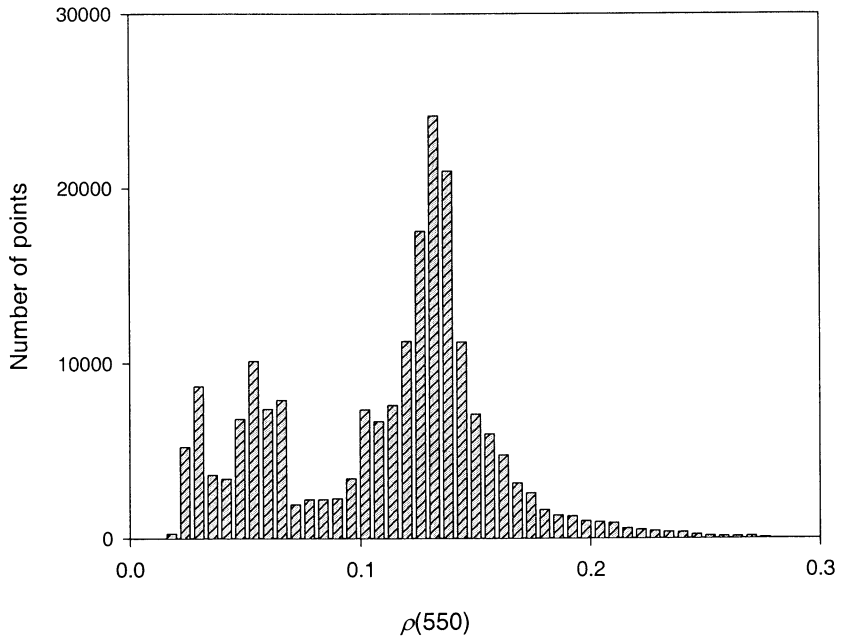

Figure 5. Histogram of $\rho(550)$ values. Clearly, we see wide variations of this value.

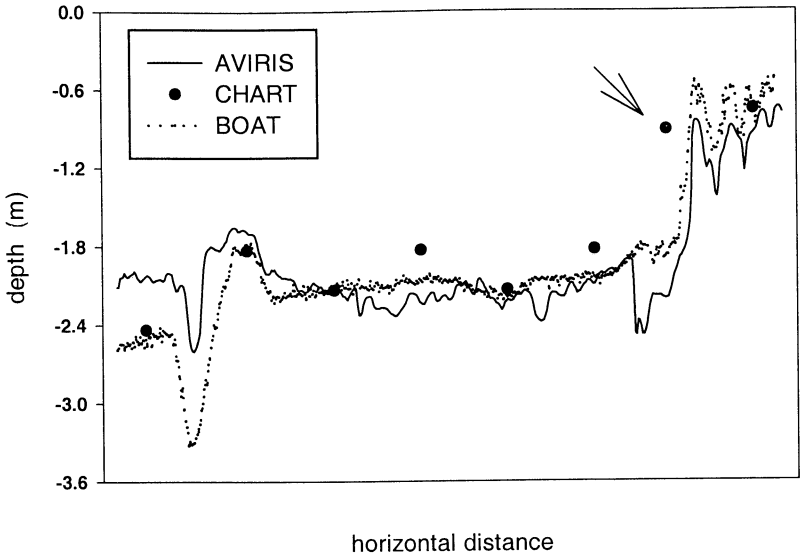

Figure 6. Depth comparison among the AVIRIS-derived, boat survey, and the National Oceanic and Atmospheric Administration (NOAA) chart data.

bar at the top left (1-2 feet, 0.3-0.6 m). (2) The shoal area near the middle left part of the image (marked B) appears to have been eroded and deepened between the time of NOAA measurements and the AVIRIS overflight (>20 years), with the area of this shoal region reduced by ~20%. The once 2-3 feet (0.6-0.9 m) area (marked B) is now 6-7 feet (1.8-2.1 m) deep (also see the arrow point in Figure 6), and the substrate has likely changed from once being grassy to now being sandy. (3) A channel has been opened at the top of the image (marked C). This place was previously uniformly ~2 feet (0.6 m) in depth, but it is now a channel with depths of ~6 feet (1.8 m).

To see how accurate the AVIRIS-derived depths were, we took a boat survey to the study area on December 8, 1999, which was ~1 year later than the AVIRIS flight. Figure 6 shows the depth comparison, which also includes a few points selected from the NOAA chart. As shown, the depth values from three sources agree with one another quite well, except that the NOAA depths appear a little bit shallower (~0.15 m), which could be due to the coarse interpolation of the NOAA depths. Except for the pixels around the deep channel shown in the boat survey (see Figure 6), the depths overall agree with each other very well. For the depth mismatch between AVIRIS and the boat survey around the deep channel it could be caused by the nearby boat (see Figure 1), with stirred-up sediments being viewed as a false bottom in the AVIRIS image. Repetitive AVIRIS coverage of the same area can overcome such uncertainties.

Putting aside the time lag between AVIRIS and boat survey (note that no major storms hit the region during that year lag) and errors in atmospheric correction, other possible sources of error include the remote-sensing reflectance model and the spectral shape of the bottom albedo used for the inversions.

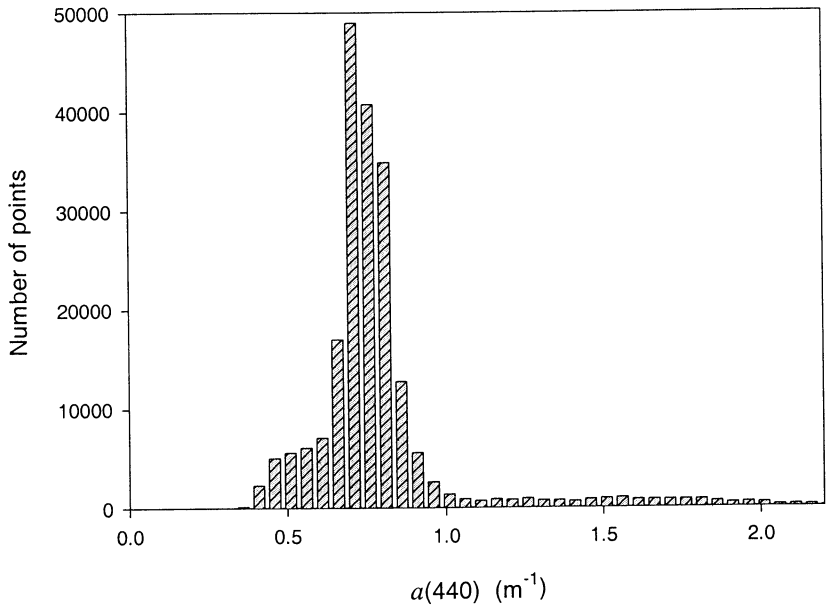

Figure 7. Histogram of $a(440)$ values. Most of the $a(440)$ values were around 0.76 m^{-1}.

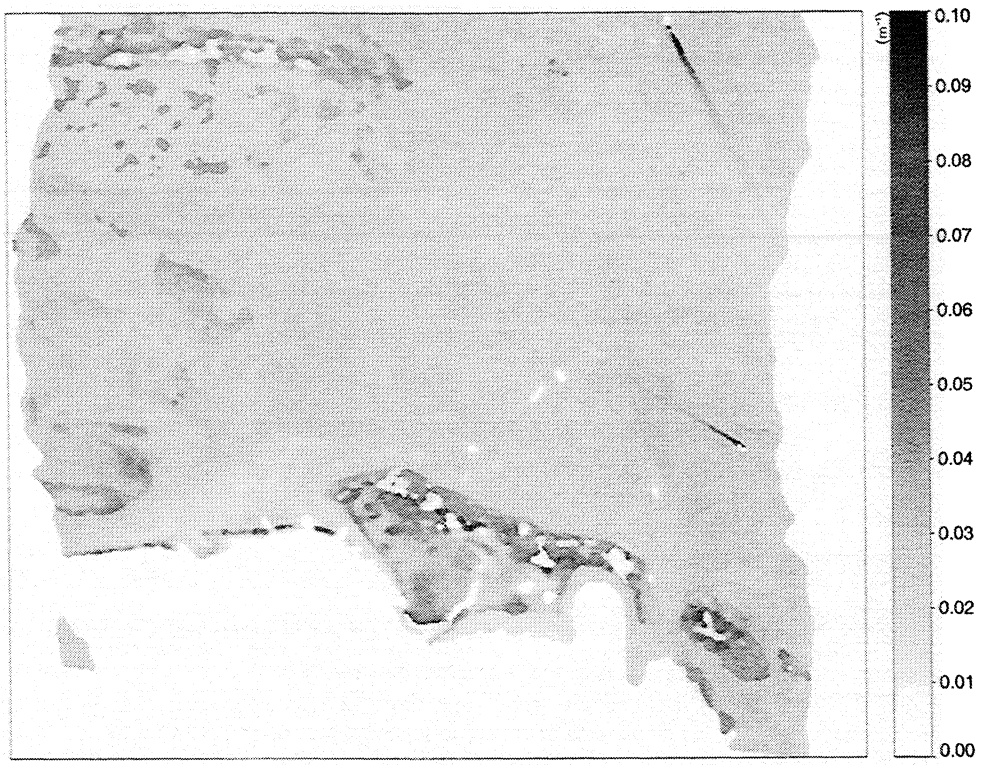

Figure 8. Image of derived particle backscattering coefficient at 400 nm.

Remember that we only used two distinctive shapes in our inversion. From pixel to pixel, however, owing to the changes in bottom composition we would expect changes also in the spectral shape of bottom albedo. Other than significant changes between grass and sand, we do not know yet how to detect subtle changes remotely. Improved algorithms and an updated database for spectral shape of the bottom albedo are needed for this region.

Plate 2b shows the image of the derived total absorption coefficient at 440 nm, while Figure 7 shows the histogram of those absorption values. More than 90% of the pixels have absorption coefficient values in a range of 0.7-0.9 m^{-1}. Highest $a(440)$ values (~1.5 m^{-1}) appeared in the shallow, lower middle part of the image (just off the city of St. Petersburg, Florida), which may be due to the very shallow water there (see Plate 1b) and perhaps due to some runoff from the city. In the middle of the image, the absorption coefficient is, in general, fairly constant, with an average value of 0.8 m^{-1}. Unfortunately, we do not have field measurements for the study image since the boat was at the atmospheric

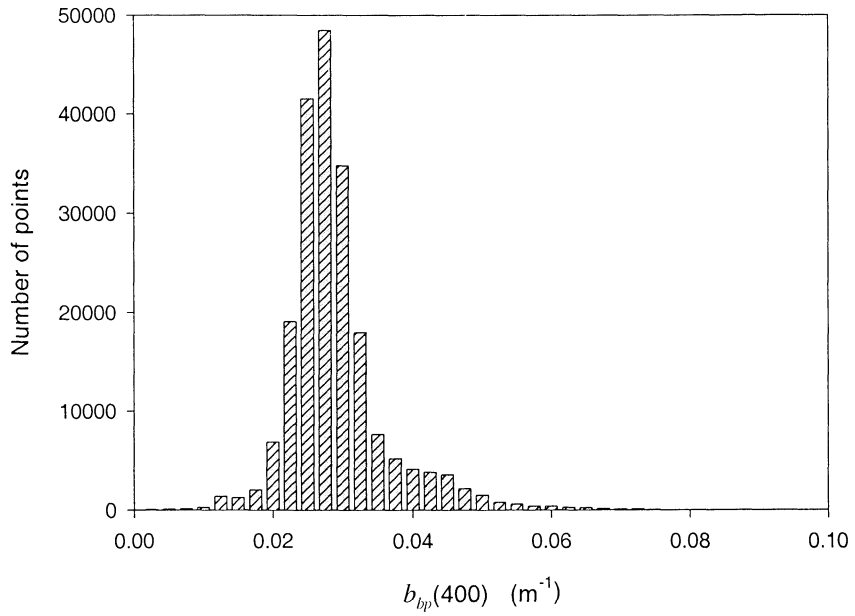

Figure 9. Histogram of $b_{bp}(400)$ values. Most of the $b_{bp}(400)$ values were around 0.027 m^{-1}.

correction/calibration site (~5 km away from this image). The $a(440)$ value, however, at the calibration site was ~0.9 m^{-1} that day, which suggests the AVIRIS-derived absorption values were quite consistent with nearby waters. More importantly, we do not see the sharp, horizontal gradients in this absorption image that appear in albedo and depth images (Plates 1a and 1b). These results suggest that the waters observed in the image appear to be well mixed horizontally, and the approach did separate clearly the causes in the radiance variation shown in Figure 1 into water column and bottom effects.

Figure 8 shows the retrieved image of the particle backscattering coefficient at 400 nm, and its histogram is shown on Figure 9. We see that most of the pixels have $b_{bp}(400)$ values between 0.02 and 0.03 m^{-1}. Clearly, this image is consistent with the $a(440)$ image in that the majority of the water body was well mixed.

With these results, we can now confidently point out that most of the radiance variation in Figure 1 was due to changes in bottom depth and bottom composition, with the water itself relatively well mixed horizontally. This is rather amazing considering that the diffuse attenuation coefficient of the water column at 440 nm is about [*Gordon et al.*, 1980] $(a+b_b)/\cos(\theta_w) \approx 1.0$ m^{-1}, and the beam attenuation coefficient at 440 nm is about $a(440) + b(440) \approx a(440) + 50\, b_b(440) \approx 2.1$ m^{-1} if we assume a 2% ratio of backscattering to total scattering (b_b/b) [see *Mobley*, 1994]. These values indicate that the waters under study are very turbid compared to clear-water regions where earlier spectral bathymetry experiments have occurred [e.g., *Lyzenga*, 1985].

5. The Influence of the Bottom on Empirical Retrievals

It has been acknowledged that empirical, spectral ratio algorithms for pigment concentrations or absorption coefficients cannot be applied to optically shallow waters. The results of applying an empirical chlorophyll a algorithm to this shoal region are shown in Figure 10. This includes chlorophyll concentrations from various retrievals along with depths for the vertical line shown in Figure 1. The empirical algorithm for chlorophyll a concentration is the OC-2 formula [*O'Reilly et al.*, 1998],

$$[C] = 10^{0.341 - 3.001\gamma + 2.811\gamma^2 - 2.041\gamma^3} - 0.04, \qquad (15)$$

with $\gamma = \log(R_{rs}(490)/R_{rs}(555))$.

In Figure 10 the left scale is for chlorophyll concentration, and the right scale is for bottom depth. Chlorophyll concentrations were calculated in three ways: (1) [C]_opt, chlorophyll concentration by optimization, was calculated from optimization-derived $a_\phi(440)$ values, using a 0.05 m^2 mg^{-1} chlorophyll-specific absorption coefficient at 440 nm (open circles); (2) [C]_dp, chlorophyll concentration for optically deep waters, was calculated using (15) after bottom effects were corrected from R_{rs} values (open triangles); and (3) [C]_sh, chlorophyll concentration for shallow waters, was calculated using (15) with raw R_{rs} values, i.e., no correction for bottom effects (open squares).

We see that the depths (solid circles) range widely from ~0.6 - 4.3 m, but [C]_opt remains ~4-5 mg m^{-3}, while 20 < [C]_dp < 30 mg m^{-3}, and 20 < [C]_sh < 100 mg m^{-3}. Though [C]_opt and [C]_dp differ significantly in absolute value, both show relatively small variations from pixel to pixel, as expected for horizontally mixed waters. On the other hand, we see strong pixel-to-pixel variations for [C]_sh, which clearly indicates the strong influence of bottom on the empirical retrieval of chlorophyll concentrations. [C]_opt retrievals do suffer sometimes from bottom effects over the very shallow (~1.2 m) grass beds area.

The variations of [C]_sh, however, are not simply correlated with the values of depth. [C]_sh provides similar values to [C]_dp for bottom depths ~1.2-1.5 m, while [C]_sh differs significantly with [C]_dp for bottom depths ~2.7 m. The reason is that OC-2 uses the ratio $R_{rs}(490)/R_{rs}(555)$. The

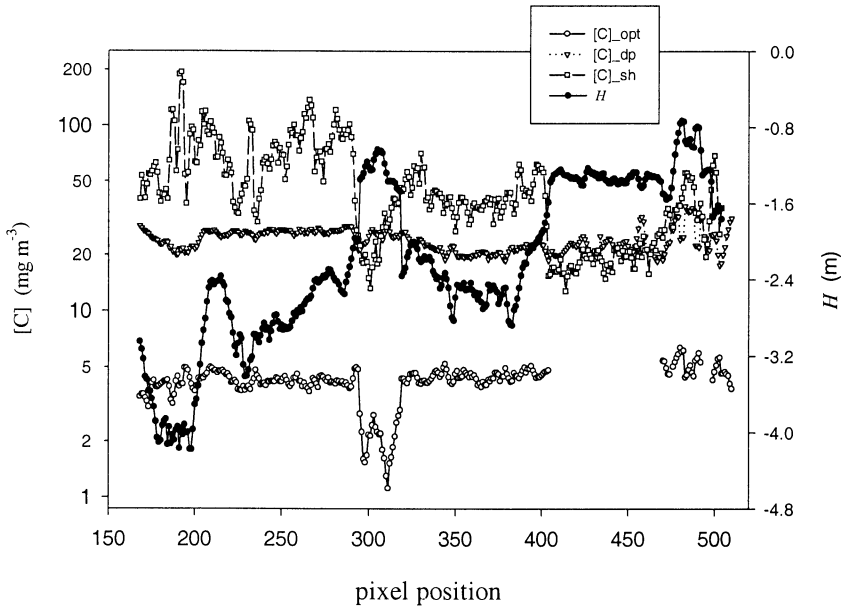

Figure 10. Comparison of retrieved chlorophyll a concentrations of a selected line. Solid circles are for depth; open circles are for values from optimization; open triangles are for values after bottom correction; and open squares are for values without bottom correction. See text for details.

influence of the bottom on this ratio (or other spectral ratios) is not just a function of depth; it is also a function of properties of water column and bottom [see *Lee et al.*, 1998]. When the bottom gets shallower, although the contribution from the bottom increases, the contribution from the water column decreases (see (2)). Depending on water and bottom constituents, the two effects sometimes compensate each other so that the $R_{rs}(490)/R_{rs}(555)$ ratio may be the same for two different depths. In this case the OC-2 derived chlorophyll concentration may be similar even though one has stronger bottom contribution than the other.

The big difference between [C]_opt and [C]_dp is the fact that the OC-2 algorithm was designed for "case 1" waters [*Morel and Prieur*, 1977], where the ratio of gelbstoff absorption to pigment absorption at 440 nm is generally ~0.8-1.2 [*Morel*, 1988, *Gordon et al.*, 1988]. For the estuary in this study, however, that ratio is as high as 5-8. As a result, the $R_{rs}(490)/R_{rs}(555)$ ratio here is largely an indicator of the gelbstoff absorption rather than pigment absorption even where bottom influence is minimal. [C]_opt values are much closer to the real values (chlorophyll concentration at the calibration site was ~5.0 mg m^{-3} on that day) as the absorption coefficients for pigments and gelbstoff were derived independently in the optimization process. The missing [C]_opt points and those with very low [C]_opt values shown in Figure 10 were due to the influence of the shallow grass beds, which limit the effectiveness of spectrally decomposing the water column signals from that due to bottom since both pigment and seagrass absorb strongly in the blue-green region.

6. Summary and Conclusions

Using a newly developed remote-sensing reflectance model and an optimization approach, AVIRIS data collected over a turbid, shallow estuary was spectrally decomposed, and properties relating to the water column and bottom were derived. The derived properties include bottom depth, bottom albedo, and absorption coefficients of the pigments and gelbstoff and backscattering coefficients of suspended particles in the water column. These derived properties were compared with historical or field measurements. It was found that the derived water column properties were quite mixed horizontally as expected, but the derived bottom depth and bottom albedo show sharp gradients and clear horizontal patterns. The depths are ranging from 0.3 to 4.6 m, and the bottom albedo at 550 nm is ranging from 2 to 30%. The depth values are consistent with a NOAA chart and a recent bathymetric survey. The albedo values are consistent with end-members of seagrass and muddy quartz sand. In certain places, the study area has changed significantly since the NOAA survey, suggesting the erosion of a grass bed and opening of an erosion channel. For some of the shallow seagrass area (~1 m in bottom depth), however, further improvements seems required for better retrieval of pigment absorption coefficient.

These results clearly indicate that (1) the semianalytical model and the optimization approach worked well in both sandy and seagrass areas, (2) the model and approach can be applied to "case 2" waters of variable depth, and (3) AVIRIS low-flight data are very useful in monitoring environmental properties of shallow coastal environments once the imagery has been vicariously calibrated and corrected for atmospheric effects. More importantly, the successful exercise here suggests that high-quality, high spectral and spatial resolution airborne imagery data can be used for environmental reconnaissance to provide guidance for future detailed ground surveys for updating bathymetric and bottom substrate maps.

If a satellite equipped with a hyperspectral sensor with 30 m resolution and enhanced signal-noise ratio such as the Coastal Ocean Imaging Spectrometer (COIS [*Davis and Carder*, 1997]) is ever funded and launched, it would provide a means to globally monitor, even in shallow waters, changes in bathymetry and benthic habitats, environmental factors indicative of eutrophication (e.g., chlorophyll *a*, absorption and scattering coefficients), and runoff. Global detection of navigational hazards, storm damage, environmental stress factors, and climate change effects (e.g., El Niño flooding) would be a boon for resource and safety management. This initial effort provides an example of the some of the applications that could be addressed by COIS if it were successfully launched.

Acknowledgments. Financial support was provided by the following contracts and grants: NASA through NAS5-97137, NAS5-31716, and NAG5-3446; the Office of Naval Research through N00014-96-I-5013, and N00014-97-0006; and the NOAA Coastal Ocean Program R/NCOP-5. The authors thank Robert Green for AVIRIS data preparation, Jennifer Patch for laboratory measurements, and two reviewers for very helpful suggestions. Z.P. Lee is grateful for the assistance and comments from M.X. He at ORSL in Qingdao Ocean University.

References

Arnone, R. A., P. Maritinolich, R. W. Gould, R. Stumpf, and S. Ladner, Coastal optical properties using SeaWiFS, *Ocean Optics XIV* [CDROM], Office of Naval Research, Arlington, 1998.

Bricaud, A., A. Morel, and L. Prieur, Absorption by dissolved organic matter of the sea (yellow substance) in the UV and visible domains, *Limnol. Oceanogr.*, *26*, 43-53, 1981.

Carder, K. L., R. G. Steward, G. R. Harvey, and P. B. Ortner, Marine humic and fulvic acids: Their effects on remote sensing of ocean chlorophyll, *Limnol. Oceanogr.*, *34*, 68-81, 1989.

Carder, K. L., S. K. Hawes, K. A. Baker, R. C. Smith, R. G. Steward, and B. G. Mitchell, Reflectance model for quantifying chlorophyll a in the presence of productivity degradation products, *J. Geophys. Res.*, *96*, 20,599-20,611, 1991.

Carder, K. L., P. Reinersman, R. F. Chen, F. Muller-Karger, C. O. Davis, and M. Hamilton, AVIRIS calibration and application in coastal oceanic environments, *Remote Sens. Environ.*, *44*, 205-216, 1993a.

Carder, K. L., R. G. Steward, R. F. Chen, S. K. Hawes, Z. P. Lee, and C. O. Davis, AVIRIS calibration and application in coastal oceanic environments: Tracers of soluble and particulate constituents of the Tampa Bay coastal plume, *Photogram. Eng. Remote Sens.*, *59*, 339-344, 1993b.

Clark, R. K., T. H. Fay, and C. L. Walker, Bathymetry calculations with Landsat 4 TM imagery under a generalized ratio assumption, *Appl. Opt.*, *26*, 4036-4038, 1987.

Davis, C. O., and K. L. Carder, Requirements driven design of an imaging spectrometer system for characterization of the coastal environment, *Proc. SPIE Int. Soc. Opt. Eng.*, *3118*, 322-329, 1997.

Gordon, H. R., R. C. Smith, and J. R. V. Zaneveld, Introduction to ocean optics, *Ocean Optics VI, Proc. SPIE Int. Opt. Soc. Eng. 208*, 1-43, 1980.

Gordon, H. R., O. B. Brown, R. H. Evans, J. W. Brown, R. C. Smith, K. S. Baker, and D. K. Clark, A semianalytic radiance model of ocean color, *J. Geophys. Res.*, *93*, 10,909-10,924, 1988.

Green, R. O., Summaries of the Eighth JPL Airborne Earth Science Workshop, *Pub. 99-17*, Jet Propul. Lab., Pasadena, Calif., 1999.

Hamilton, M. K., C. O. Davis, W. J. Rhea, S. H. Pilorz, and K. L. Carder, Estimating chlorophyll content and bathymetry of Lake Tahoe using AVIRIS data, *Remote Sens. Environ.*, *44*, 217-229, 1993.

Hou, W. L., L. Renadette, A. Farmer, K. L. Carder, D. Costello, and T. G. Peacock, Bottom reflectance of various benthic types based on in-situ multi-channel imagery, *Eos Trans. AGU, 80*(49), Ocean Sci. Meet. Suppl., OS22E-14, 2000.

Lee, Z. P., Visible-infrared remote-sensing model and applications for ocean waters, Ph.D. dissertation, Univ. of South Florida, St. Petersburg, 1994.

Lee, Z. P., K. L. Carder, S. K. Hawes, R. G. Steward, T. G. Peacock, and C. O. Davis, A model for interpretation of hyperspectral remote sensing reflectance, *Appl. Opt., 33*, 5721-5732, 1994.

Lee, Z. P., K. L. Carder, C. D. Mobley, R. G. Steward, and J. S. Patch, Hyperspectral remote sensing for shallow waters, 1, A semi-analytical model, *Appl. Opt., 37*, 6329-6338, 1998.

Lee, Z. P., K. L. Carder, C. Mobley, R. G. Steward, and J. S. Patch, Hyperspectral remote sensing for shallow waters, 2, Deriving bottom depths and water properties by optimization, *Appl. Opt., 38*, 3831-3843, 1999.

Lyzenga, D. R., Passive remote-sensing techniques for mapping water depth and bottom features, *Appl. Opt., 17*, 379-83, 1978.

Lyzenga, D. R., Remote sensing of bottom reflectance and water attenuation parameters in shallow water using aircraft and Landsat data, *Int. J. Remote Sens., 2*, 71-82, 1981.

Lyzenga, D. R., Shallow-water bathymetry using combined lidar and passive multispectral scanner data, *Int. J. Remote Senss., 6*, 115-125, 1985.

Marshall, B. R., and R. C. Smith, Raman scattering and in-water ocean properties, *Appl. Opt., 29*, 71-84, 1990.

Mobley, C. D. *Light and Water: Radiative Transfer in Natural Waters*, Academic, San Diego, Calif. 1994.

Morel, A., Optical properties of pure water and pure sea water, in *Optical Aspects of Oceanography*, edited by. N. G. Jerlov and E. S. Nielsen, pp. 1-24, Academic, San Diego, Calif., 1974.

Morel, A., Optical modeling of the upper ocean in relation to its biogenous matter content (case I waters), *J. Geophys. Res., 93*, 10,749-10,768, 1988.

Morel, A., and B. Gentili, Diffuse reflectance of oceanic waters (2): Bi-directional aspects, *Appl. Opt., 32*, 6864-6879, 1993.

Morel, A., and L. Prieur, Analysis of variations in ocean color, *Limnol. Oceanogr., 22*, 709-22, 1977.

Mueller, J. L., and R. W. Austin, Ocean optics protocols for SeaWiFS validation, *NASA Technical Memo., 104566*, 1992.

O'Neill, N. T., and J. R. Miller, On calibration of passive optical bathymetry through depth soundings analysis and treatment of errors resulting from the spatial variation of environmental parameters, *Int. J. Remote Sens. 10*, 1481-1501, 1989.

O'Reilly, J. E., S. Maritorena, B. G. Mitchell, D. A. Siegel, K. L. Carder, S. A. Garver, M. Kahru, and C. McClain, Ocean color chlorophyll algorithms for SeaWiFS, *J. Geophys. Res., 103*, 24,937-24,953, 1998.

Paredes, J. M., and R. E. Spero, Water depth mapping from passive remote sensing data under a generalized ratio assumption, *Appl. Opt., 22*, 1134-1135, 1983.

Philpot, W. D., Bathymetric mapping with passive multispectral imagery, *Appl. Opt., 28*, 1569-1578, 1989.

Polcyn, F. C., W. L. Brown, and I. J. Sattinger, The measurement of water depth by remote-sensing techniques, Rep. 8973-26-F, Willow Run Lab., Univ. of Mich., Ann Arbor, 1970.

Pope, R., and E. Fry, Absorption spectrum (380 - 700nm) of pure waters, II, Integrating cavity measurements, *Appl. Opt., 36*, 8710-8723, 1997.

Preisendorfer, R. W., *Hydrologic optics*, vol. 1: *Introduction, NTIS PB-259 793/8ST*, Nati. Tech. Inf. Serv., Springfield, Va., 1976.

Roesler, C. S., M. J. Perry, and K. L. Carder, Modeling in situ phytoplankton absorption from total absorption spectra in productive inland marine waters, *Limnol. Oceanogr., 34*, 1510-1523, 1989.

Sathyendranath, S., L. Prieur, and A. Morel, A three-component model of ocean colour and its application to remote sensing of phytoplankton pigments in coastal waters, *Int. J. Remote Sens., 10*, 1373-1394, 1989.

Zhang, M. R., K. L. Carder, Z. P. Lee, F. E. Muller-Karger, and D. B. Goldgof, "Noise reduction and atmospheric correction for coastal applications of LANDSAT thematic mapper imagery, *Remote Sens. Environ., 70*, 167-180, 1999.

K. L. Carder, R. F. Chen, Z. P. Lee, and T. G. Peacock, Department of Marine Science, University of South Florida, 140 7th Ave. S., St. Petersburg, FL 33701. (zplee@monty.marine.usf.edu.)

(Received July 17, 2000; revised December 15, 2000;
accepted February 2, 2001.)